

Functional Redundancy in *Candida auris* Cell Surface Adhesins Crucial for Cell-Cell Interaction and Aggregation

Tristan W. Wang¹, Dimitrios Sofras², Daniel Montelongo-Jauregui¹, Telmo O. Paiva³, Hans Carolus², Yves F. Dufrêne³, Areej A. Alfaifi^{1*}, Carrie McCracken⁴, Vincent M. Bruno⁵, Patrick Van Dijck^{2*}, Mary Ann Jabra-Rizk^{1,5*}

¹⁰ ¹¹ ¹ Department of Oncology and Diagnostic Sciences, School of Dentistry, University of Maryland, Baltimore, MD 21201, USA

13 ²Laboratory of Molecular Cell Biology, Department of Biology, KU Leuven, Leuven, Belgium

¹⁴ ³ Louvain Institute of Biomolecular Science and Technology, UCLouvain, Croix du Sud, 4-5,
¹⁵ L7.07.07, B-1348 Louvain-la-Neuve, Belgium

17 ⁴ Institute for Genome Sciences, University of Maryland School of Medicine, Baltimore, MD
18 21201, USA.

20 ⁵ Department of Microbiology and Immunology, School of Medicine University of Maryland,
21 Baltimore, MD 21201, USA

Current affiliation: Department of Restorative and Prosthetic Dental Sciences, College of Dentistry King Saud bin Abdulaziz University for Health Sciences, Rivadh, Saudi Arabia

Current affiliation: Department of Restorative and Prosthetic Dental Sciences, College of Dentistry King Saud bin Abdulaziz University for Health Sciences, Riyadh, Saudi Arabia

* Corresponding authors:

Mary Ann Jabra-Rizk, Ph.D.
University of Maryland-Baltimore, School of Dentistry,
650 W. Baltimore Street, 7 North #7253
Baltimore, Maryland 21201
Phone: 410-706-0508
Fax: 410-706-0519
Email: mrizk@umaryland.edu

Patrick Van Dijck, Ph.D.
Laboratory of Molecular Cell Biology,
Department of Biology,
KU Leuven, Leuven, Belgium
Email: Patrick.vandijck@kuleuven.be

46 **ABSTRACT**

47

48 *Candida auris* is an emerging nosocomial fungal pathogen associated with life-threatening
49 invasive disease due to its persistent colonization, high level of transmissibility and multi-drug
50 resistance. Aggregative and non-aggregative growth phenotypes for *C. auris* strains with
51 different biofilm forming abilities, drug susceptibilities and virulence characteristics have been
52 described. Using comprehensive transcriptional analysis we identified key cell surface adhesins
53 that were highly upregulated in the aggregative phenotype during *in vitro* and *in vivo* grown
54 biofilms using a mouse model of catheter infection. Phenotypic and functional evaluations of
55 generated null mutants demonstrated crucial roles for the adhesins Als5 and Scf1 in mediating
56 cell-cell adherence, coaggregation and biofilm formation. While individual mutants were largely
57 non-aggregative, in combination cells were able to co-adhere and aggregate, as directly
58 demonstrated by measuring cell adhesion forces using single-cell atomic force spectroscopy.
59 This co-adherence indicates their role as complementary adhesins, which despite their limited
60 similarity, may function redundantly to promote cell-cell interaction and biofilm formation.
61 Functional diversity of cell wall proteins may be a form of regulation that provides the aggregative
62 phenotype of *C. auris* with flexibility and rapid adaptation to the environment, potentially
63 impacting persistence and virulence.

64

65 **INTRODUCTION**

66 The newly emerged nosocomial pathogen *Candida auris* is associated with outbreaks of
67 life-threatening invasive disease worldwide¹⁻⁴. *Candida auris* exhibits several concerning
68 features including persistent colonization of skin and nosocomial surfaces, high transmissibility
69 and unprecedented level of multi-drug resistance⁵⁻¹¹. In fact, *C. auris* is now the first fungal
70 pathogen categorized as an urgent threat by the Center for Disease Control (CDC), making it
71 mandatory to report isolation of *C. auris* in the United States^{10,12}. Significantly, the World Health
72 Organization ranks *C. auris* as a critical priority pathogen, highlighting its importance to public
73 health¹³. While virulence factors associated with *C. auris* infections are not fully understood, the
74 fungus shares key characteristics common to *Candida* species including thermotolerance and
75 biofilm formation, although some characteristics are strain-dependent^{10,14-16}. Biofilm formation
76 contributes to antifungal tolerance among *Candida* species as a result of drug sequestration,
77 and in *C. auris*, biofilm formation was shown to protect *C. auris* from triazoles, polyenes, and
78 echinocandins¹⁷⁻¹⁹. One unique growth feature reported in some clinical isolates is cell
79 aggregation, which *in vitro* was associated with differences in drug susceptibility and
80 transcriptional changes induced by exposure to antifungals²⁰. Aggregative isolates were also
81 shown to have higher capacity for biofilm formation than non-aggregative isolates^{16,18, 20-22}.

82

83 Fungal cell wall adhesins are crucial for adherence to surfaces and biofilm formation and
84 have been recognized as major virulence factors in *Candida* species²³. Adhesins also play a
85 fundamental role in interactions of fungal cells with each other enabling switching from a
86 unicellular lifestyle to a multicellular one¹⁸. In *Candida*, most notably, cell adhesion involves a
87 family of cell surface Als (agglutinin-like sequence) proteins with amyloid-like clusters that
88 activate cell-cell adhesion under mechanical stress^{24,25}. Identified polymorphisms enriched in
89 weakly-aggregating strains of *C. auris* were found to be associated with loss of cell surface
90 proteins; furthermore, amplification of the subtelomeric adhesin gene *ALS4* was associated with
91 enhanced adherence and biofilm formation^{26,27}. In addition, cell aggregation was shown to

92 increase at higher growth temperatures, suggesting that aggregation is a complex phenomenon
93 that may be linked to the ability to form extracellular matrix and cell surface amyloids^{26,28}.
94

95 In this study, we aimed to identify unique transcriptional signatures associated with the
96 aggregative phenotype during biofilm growth. As the *in vivo* and *in vitro* situations may have
97 different functional requirements, comparative RNA sequencing analysis was performed on *C.*
98 *auris* strains grown *in vitro* and *in vivo* using our mouse model of catheter infection. Analysis of
100 differentially regulated genes identified key cell wall adhesin genes to be significantly
101 upregulated in the aggregative strain, and functional analysis of generated null mutants identified
102 an adhesin important for biofilm formation *in vivo*. As complementary roles for diverse adhesins
103 have been reported in *C. albicans*²⁹, we aimed to explore adhesin functional redundancy and
104 binding complementation in *C. auris*, which was demonstrated by measuring cell-cell adhesive
105 forces using single-cell atomic force spectroscopy. Functional diversity of cell wall proteins may
106 be a form of regulation providing the *C. auris* aggregative phenotype with flexibility and rapid
107 adaptation to the environment. Therefore, dissecting this aggregative phenotype is crucial for
108 understanding the biology, evolution and pathogenesis of *C. auris*.
109

RESULTS

111 **Transcriptional analysis identifies key cell wall adhesins to be significantly upregulated**
112 **in an aggregating *C. auris* strain under both *in vitro* and *in vivo* growth conditions.** To
113 understand the molecular mechanisms behind the differences observed in the biofilm forming-
114 ability of the two *C. auris* phenotypes, comprehensive RNA-sequencing analysis was performed
115 on cells from *in vitro* grown biofilms. A total of 76 genes were identified to be differentially
116 expressed (LFC $\geq |1|$, FDR < 0.01) between the aggregative AR0382 (B11109) and non-
117 aggregative AR0387 (B8441) strains (Fig. 1A); 47 of the genes were more highly expressed in
118 AR0382, whereas 29 genes were more highly expressed in AR0387. Transcriptional analysis of
119 *in vivo* grown biofilms recovered from catheters implanted in mice identified 259 genes that were
120 differentially expressed (LFC $\geq |1|$, FDR < 0.01) between AR0382 and AR0387 (Fig.1B); 206 of
121 the genes were more highly expressed in strain AR0382 whereas 53 genes were more highly
122 expressed in AR0387 (Supplementary Table S1 and S2). 23 genes were commonly more highly
123 expressed in AR0382 *in vitro* and *in vivo* (Fig. 1C) (Table S3); among those genes, 5 encode
124 putative adhesins, including B9J08_001458 and B9J08_004112, which have since been
125 annotated as *SCF1* and *ALS5*, respectively. Additionally identified were several homologs of *C.*
126 *albicans* genes with known roles in adhesion including: B9J08_004109 (*IFF4109*) and
127 B9J08_004100 and B9J08_004451 belonging to the *IFF/HYR1* family of adhesins (Fig.1A, B).
128 Interestingly, gene B9J08_002136, an ortholog of the *C. albicans* transcription factor *WOR2* and
129 key regulator of white-to-opaque switching³⁰, was significantly underexpressed in strain AR0382
130 under both growth conditions (Fig.1A, B). In this study, we focused on the two adhesins, *Scf1*
131 and *Als5*.
132

133 **The *C. auris* *Scf1* adhesin contains a *Flo11* protein domain and a serine-threonine rich**
134 **region similar to the *C. albicans* *Rbt1* adhesin.** We initially identified gene B9J08_001458 as
135 an ortholog of the *C. albicans* *RBT1* gene in agreement with a previous report³¹; however, this
136 gene has since been renamed *SCF1*²⁸. In exploring the similarity between the *C. auris* *Scf1* and
137 the *C. albicans* *Rbt1* adhesin, comparative analysis of protein domain organization was

138 performed. This revealed a comparable structure for *C. auris* Scf1 to that of the *C. albicans* Rbt1
139 and the *S. cerevisiae* Flo11 adhesins; specifically, a Flo11 domain and a serine-threonine rich
140 region recognized by Als5, were present in all 3 proteins (Fig. 2).

141
142 **Mutant strain Δ scf1 but not Δ als5 is compromised in *in vitro* biofilm formation compared**
143 **to the wild-type strain.** Quantitative evaluation of biofilms based on metabolic activity
144 demonstrated that the Δ scf1 mutant formed significantly reduced biofilm compared to the wild-
145 type strain. In contrast, the Δ als5 biofilm was comparable to that of the wild-type (Fig 3A). The
146 non-aggregative AR0387 wild-type strain was severely deficient in biofilm formation compared
147 to AR0382, and deletion of either gene in AR0387 had no additional effect on adhesion and
148 biofilm formation (Fig. S1A).

149
150 **Both mutant strains Δ scf1 and Δ als5 are significantly deficient in aggregation.** Following
151 vortexing of cell suspensions, the AR0382 wild-type strain formed large aggregates rapidly
152 settling into a sediment (Fig. 3B, C). In contrast, mutants lacking the Scf1 or Als5 adhesins
153 formed no or minimally visible aggregates and cells remained mostly suspended (Fig. 3B, C).
154 Comparative measurement of sedimentation rates of aggregates based on drop in absorbance
155 readings over time demonstrated that unlike with the Δ scf1 and Δ als5 mutants, the drop in
156 absorbance for the wild-type strain was dramatic (Fig. 3D). No aggregation was seen with cells
157 of the AR0387 wild-type strain (Fig. S1B-C).

158
159 **Scf1 and Als5 adhesins have complementary and redundant roles in cell-cell adherence**
160 **and aggregation.** In order to explore whether the two highly expressed adhesins in the
161 aggregative strain have complementary roles, the two mutant strains were mixed and cell-cell
162 adherence and coaggregation were monitored visually and quantitatively. Where individually
163 both mutants failed to aggregate, in combination, cells co-adhered strongly, forming aggregates
164 comparable to those formed by the wild-type strain (Figs. 3B-D).

165
166 **Confocal Laser Scanning Microscopy (CLSM) and Scanning Electron Microscopy (SEM)**
167 **imaging reveal significant differences in biofilm architecture for Δ scf1 and Δ als5**
168 **compared to the wild-type and Δ scf1+ Δ als5 mixed biofilm.** CLSM images revealed
169 significant differences in the extent and structure of biofilms formed by the wild-type and Δ scf1;
170 where the wild-type biofilm consisted of dense matrix and cell aggregates, the Δ scf1 biofilm was
171 patchy and less dense (Fig. 4). Although Δ als5 formed a substantial biofilm, it was not as dense
172 or aggregative as the wild-type. In contrast, biofilm formed by combination of Δ als5 and Δ scf1
173 was comparable to that of the wild-type. SEM analysis revealed similar biofilm structures where
174 wild-type and Δ als5+ Δ scf1 mixed biofilms consisted of piles of cell aggregates, and biofilms of
175 Δ als5 and Δ scf1 were homogenous consisting mostly of single layer of cells (Fig. 5).

176
177 **Atomic force microscopy (AFM) reveals major differences in cell-cell adhesion forces**
178 **between the different strains.** Force-distance curves recorded by AFM³² between two AR0382
179 wild-type cells featured a large adhesion force peak averaged at 338 ± 219 pN (mean \pm standard
180 deviation (SD), $n = 1567$ adhesive curves from 6 cell combinations) (Fig. 6A, B). Moreover, some
181 force profiles showed sawtooth patterns with multiple force peaks in the 200-500 pN range,
182 which could be attributed to the sequential unfolding of the tandem repeat domains of Als
183 proteins³³ (Fig. 2). Interestingly, a wide distribution of adhesion forces, composed of both weak

184 and strong forces was observed for this strain. In the non-aggregative AR0387 strain however,
185 intercellular adhesion was essentially non-existent (4%) and only weak forces of 96 ± 29 pN (305
186 adhesive curves from 4 cell pairs) were measured (Fig. S1 D-F). In contrast to AR0382,
187 significant decrease in adhesion frequency was observed for the $\Delta als5$ strain (from 80% to 30%)
188 (Fig. 6C), where force curves featured only weak adhesion forces of 127 ± 27 pN (n = 608
189 adhesive curves from 6 cell pairs) (Fig. 6B), and sawtooth patterns were not observed (Fig. 6A).
190 Similar intercellular adhesion forces were measured for the $\Delta scf1$ strain (111 ± 30 pN, n = 731
191 adhesive curves from 6 cell pairs), and an adhesion frequency slightly higher than what was
192 observed for the $\Delta als5$ strain (46%) Fig. 6C). Finally, adhesion was also probed between cells
193 of the $\Delta als5$ and $\Delta scf1$ mutants; even though a mean adhesion frequency of 54% was registered
194 (Fig. 6C), half of the cell pairs probed exhibited adhesion frequency in the same range of what
195 was observed for the AR0382 wild-type strain. Despite this difference, intercellular adhesion
196 forces of 132 ± 43 pN (n = 1146 adhesive curves from 8 cell combinations) were measured for
197 the $\Delta als5+\Delta scf1$ experiment (Fig. 6A, B).
198

199 **SEM analysis of catheters implanted in mice showed impaired *in vivo* biofilm formation**
200 **in $\Delta scf1$ mutant compared to wild-type strains.** SEM imaging of Infected catheters recovered
201 from mice (Fig. 7A) revealed significant differences in density and architecture of biofilms formed
202 within catheter lumens. The AR0382 wild-type strain formed a robust biofilm consisting of
203 aggregates of cells; in contrast, biofilms within catheters infected with $\Delta scf1$ were scarce with
204 patches consisting primarily of extracellular matrix with fewer yeast cells in single layers and no
205 or minimum cell aggregates, comparable to that formed by the non-aggregative AR0387 wild-
206 type strain (Fig. 7B).
207

208 **DISCUSSION**

209

210 *Candida auris* avidly adheres and forms biofilms on indwelling medical devices such as
211 intravascular catheters, an important risk factor for systemic infection. A striking morphological
212 feature of some *C. auris* isolates is their capacity to aggregate and form strong biofilms^{18,27}. In
213 this study, we performed comprehensive comparative analysis of biofilms formed by strains
214 exhibiting a high and low aggregation phenotype under *in vitro* and *in vivo* growth conditions.
215 First, our analysis focused on identifying genes that were more highly expressed in the
216 aggregative strain both *in vitro* and *in vivo*, specifically those with predicted roles in adhesion
217 and biofilm formation based on functional homology in other *Candida* species. Most notable
218 among the genes that are more highly expressed in the aggregative strain were B9J08_001458
219 and B9J08_004112, which encode homologs of *C. albicans* *RBT1* and *ALS5*, respectively^{31,34,}
220 ³⁵. Recently, B9J08_001458 was described as unique to *C. auris* and was named *SCF1* by
221 Santana *et al.*^{28,36}; protein domain analysis shows that both *Scf1* and *Saccharomyces cerevisiae*
222 *Flo11p* share a N-terminal *Flo11* domain²⁸. The *Flo* adhesin family initially discovered in brewer's
223 yeast (*S. cerevisiae*) has the ability to form cellular aggregates induced by shear force^{18,29}.
224 Interestingly, we identified a *Flo11* domain in the *C. albicans* *Rbt1* in the N-terminal domain and
225 sequence comparisons demonstrated high similarities between the *Flo11* domains of the *C.*
226 *auris* *Scf1* and *C. albicans* *Rbt1* (Fig. 2). The *C. albicans* *Rbt1* adhesin is involved in cell-cell
227 adhesion and overexpression of *RBT1* in *C. albicans* was shown to trigger the clustering of other
228 cell surface proteins harboring aggregate-forming sequences such as *Hwp1*, by forming
229

230 intermolecular bonds^{31,37}. Further, Rbt1 is related to the Hwp1 and Hwp2 cell wall proteins that
231 play distinct but overlapping roles in *C. albicans* for promoting biofilm formation³⁸. In fact, the
232 Hwp1 protein possesses an internal serine-threonine-rich region with a critical role in cell-cell
233 adhesion and biofilm formation³⁹. Therefore, we propose that Scf1 functions as an adhesin in a
234 similar manner to the *C. albicans* Rbt1 and Hwp1.
235

236 Fungal cellular aggregation is proposed to occur as a result of a global cell surface
237 conformational shift⁴⁰. Therefore, we aimed to investigate the contribution of the *C. auris* Scf1 in
238 relation to other expressed adhesins, primarily the co-upregulated Als5. Heterologous
239 expression of the *C. albicans* Als5 at the surface of *S. cerevisiae* was shown to result in Als5-
240 mediated adhesion followed by formation of multicellular aggregates, which was not observed
241 when *ALS5* was expressed at reduced levels^{41,42}. In exploring the mechanism driving Als5-
242 mediated intercellular adhesion, a study described an aggregation mechanism whereby amyloid
243 core sequences in Als proteins trigger the formation of cell surface adhesion nanoclusters,
244 facilitating strong interactions between adhesins on opposing cells²⁵. Interestingly, in *C.
245 albicans*, Als5 adhesion was shown to be mediated by recognition of a minimum of four
246 accessible contiguous threonine and serine residues^{43,44}. Our analysis of the Scf1 protein
247 sequence identified the presence of five contiguous Als5-recognized threonine-serine rich
248 domains comparable to that in the *C. albicans* Hwp1 and Rbt1, further supporting the functional
249 similarity of Scf1 to this class of *C. albicans* adhesins (Fig. 2). This degenerate “recognition
250 system” among adhesins would provide *C. auris* with a plethora of target proteins for
251 adherence⁴⁴.
252

253 Interestingly, complementary roles for *C. albicans* Hwp1 and Als1/3 in biofilm formation
254 have been described by Nobile *et al.*²⁹, whereby a mixture of biofilm-defective *HWP1* and *ALS1/3*
255 mutants could form a hybrid biofilm. Hence similarly, despite their sequence divergence, we
256 posit that in *C. auris*, Als5 and Scf1 may function redundantly to promote cell-cell interaction and
257 biofilm formation (Fig. 8). To that end, we generated gene deletion strains of *C. auris* *SCF1* and
258 *ALS5* in the aggregative strain AR0382. Interestingly, phenotypic evaluations demonstrated
259 reduced adhesion and biofilm formation *in vitro* for the Δ *scf1* mutant, but not for the Δ *als5* mutant
260 compared to the wild-type strain (Fig. 3A). Individually, cells of Δ *scf1* and Δ *als5* lost aggregation
261 capability, but aggregation was restored when combined (Fig. 3B-D). This aggregation was also
262 demonstrated by SEM analysis, revealing a confluent mixed biofilm comprised of heaps of co-
263 adhering cells, comparable to that seen with the wild-type (Fig. 5). Interestingly however,
264 although based on assessment of metabolic activity the Δ *als5* biofilm was comparable to that of
265 the wild-type, SEM biofilm imaging revealed dramatic structural differences. These observations
266 corroborate a previous report that Als5 is not crucial for adherence to abiotic surfaces²⁸.
267 However, here we show that this adhesin is necessary for mediating cell-cell adherence. Due to
268 the observed reduction in the ability of Δ *scf1* to form biofilm *in vitro*, we then tested this mutant
269 in our mouse model to evaluate biofilm formation *in vivo*. In contrast to the dense aggregative
270 biofilm formed by the AR0382 strain, SEM imaging of the biofilms within catheters revealed a
271 minimal biofilm formed by Δ *scf1*, comparable to that of the AR0387 strain consisting primarily of
272 single layers of yeast cells, (Fig. 7).
273

274 The strong cell-cell affinities between the Δ *scf1* and Δ *als5* mutants were assessed by
275 measuring adhesion forces using single-cell force spectroscopy (Fig. 6 and Fig. S1). With the

wild-type strain, a wide distribution of adhesion forces composed of both weak and strong forces were detected, indicative of a complex binding mechanism that involves a combination of single and multiple molecular bonds. The involvement of the Als5 and Scf1 adhesin in cell-cell adhesion was demonstrated by the significant decrease in adhesion frequency observed between cells of the Δ als5 and Δ scf1 strain, which was partially restored by mixing the two deletion strains. High forces were not completely restored however when probing Δ als5 cells with Δ scf1 cells (and vice versa), indicating that *C. auris* cell-cell adhesion not only involves a combination of single and multiple Als5-Scf1 bonds, but also Als5-Als5 and Scf1-Scf1 homophilic bonds, and potentially other mechanisms (Fig. 8). In fact, it is well-documented for *C. albicans* that Als5 proteins are able to form intercellular amyloid bonds through their T domains to promote biofilm formation^{25, 33,45,46}. Additionally, since the *C. albicans* Rbt1 was also shown to be capable of forming amyloid bonds^{37,47}, it is tempting to speculate that similar homophilic binding might similarly occur with the *C. auris* Scf1 adhesin. Combined, these findings indicate that Als5 and Scf1 undergo a complementary heterophilic binding reaction that supports *C. auris* cell-cell adherence, critical for intraspecies adhesin interactions and promoting formation of monospecies biofilms.

Collectively, our findings demonstrated significant *in vitro* and *in vivo* transcriptional changes associated with the *C. auris* aggregative form impacting cell wall adhesins that although with little similarity, may have complementary roles, and function redundantly to promote cell-cell interaction and biofilm formation (Fig. 8). Functional diversity of cell wall proteins may be a form of regulation providing the *C. auris* aggregative phenotype with flexibility and rapid adaptation to the environment, potentially impacting persistence and virulence

METHODS

Strains and growth conditions. The *C. auris* wild-type strains AR0382 (B11109) and AR0387 (B8441) from the CDC AR-panel were used as wild-type strains in this study. We have previously characterized these strains and designated AR0382 as aggregative/high biofilm former and AR0387 as non-aggregative/low biofilm former¹⁶. Both isolates were confirmed to belong to clade I (East Asian) based on Carolus *et al.*⁴⁸ and were isolated in Pakistan; AR0382 was recovered from a burn wound and AR0387 from blood. Mutant strains of *C. auris* genes B9J08_001458 and B9J08_004112 in the AR0387 and AR0382 backgrounds were generated in this study. These genes have since been named SCF1 and ALS5, respectively^{27,28}. Isolates were grown overnight in yeast peptone dextrose broth (YPD) (Difco Laboratories) at 30°C, washed in Phosphate Buffered Saline (PBS) and resuspended in PBS to final cell density needed.

In vitro transcriptional analysis of AR0387 and AR0382 biofilms using RNA-sequencing. Biofilms of both wild-type strains were formed in 6-well plates in RPMI 1640-HEPES media (Invitrogen) at 37°C for 24 h. Following incubation, wells were rinsed with PBS and biofilms were scraped. Recovered cells were snap-frozen on dry ice and ethanol, allowed to thaw at room temperature (RT), then incubated for 30 min at 37°C in “digestion buffer” containing 100 U/ml of lyticase and RNase inhibitor in TRIS-EDTA 1x buffer. RNA was extracted in 1 ml of TRI Reagent™ Solution (Ambion, Invitrogen; Carlsbad, CA) using bead-beating for 30 min at RT followed by purification using Direct-zol RNA Miniprep kit (Zymo Research; Tustin, CA). Eluted RNA was analyzed in a Nanodrop Lite (Thermo Scientific). Total RNA was subjected to rRNA

322 depletion with the Ribominus Eukaryote Kit. All RNA-seq libraries (strand-specific, paired end)
323 were prepared with the TruSeq RNA sample prep kit (Illumina). One hundred nucleotides of
324 sequence were determined from both ends of each cDNA fragment using the Novaseq platform
325 (Illumina). Sequencing reads were aligned to the reference genomes (*C. auris* strain B8441)
326 using HISAT2⁴⁹, and alignment files were used to generate read counts for each gene; statistical
327 analysis of differential gene expression was performed using the DEseq package from
328 Bioconductor⁵⁰. A gene was considered differentially expressed if the absolute log fold change
329 was greater than or equal to 1 and the FDR value for differential expression was below 0.01.
330 The RNA-seq analysis was performed in biological triplicate. Given the limited annotation of the
331 *C. auris* genome, some of the gene names reported are based on homology to *C. albicans*
332 genes. For genes with no recognizable orthologs, the original systematic *C. auris* gene
333 designation is provided.

334

335 ***In vivo* transcriptional analysis of AR0387 and AR0382 biofilms formed within catheters**
336 **implanted in mice using RNA-sequencing.** All animal experiments were conducted at the
337 AAALAAC accredited Animal Facility of the University of Maryland, Baltimore and were approved
338 by Animal Care and Use Committee. Three-month-old female Balb/c mice (Jackson Laboratory)
339 were housed at a maximum of 5 per cage, weighed and closely monitored for any signs of
340 distress. A modified model previously described by Kucharíková *et al.*⁵¹ was used; 0.5 cm
341 fragments of polyurethane triple-lumen central venous catheters (Jorgensen Laboratories) pre-
342 coated overnight with fetal bovine serum (GibcoTM) were incubated with 1x10⁸ cells/ml cell
343 suspensions in PBS for 1.5 h at 37°C, rinsed and kept on ice until implanted. For each
344 experimental set, *in vitro*-infected catheters were processed for assessment of microbial
345 recovery. Mice were anesthetized with 0.5 ml intraperitoneal injections of tribromoethanol (TBE)
346 solution (250 mg/kg; Sigma-Aldrich); dorsum of mice was shaved and a small incision made
347 aseptically and a subcutaneous tunnel was created allowing for insertion of up to 5 pieces of
348 pre-inoculated catheters (Fig. 7A). Incisions were sealed using 3M VetbondTM tissue glue and
349 lidocaine analgesic gel was applied. Biofilms were allowed to form within catheters for 72 h then
350 animals were euthanized by CO₂ inhalation followed by cervical dislocation. Catheters were
351 collected in RNAlater buffer, aseptically fragmented, sonicated in RNase free water and cells
352 from all catheters recovered from each mouse were pooled by centrifugation. RNA-sequencing
353 was performed as described above. The AR0382 group contained three biological replicates
354 and the AR0387 group contained four biological replicates. A total of 40 mice were used.

355

356 **Generation of mutant strains of genes B9J08_001458 (SCF1) and B9J08_004112 (ALS5).**
357 *Plasmid construction.* The plasmids used in this study were propagated in *E. coli*
358 TOP10F'chemically competent cells. Bacterial transformations were carried out by heat shock
359 at 42°C for 45 sec using 30 µl of competent cells, and subsequent cooling on ice for 2 min. The
360 transformants were selected on solid LB (Sigma, Fisher Scientific) medium (agar 15%, BactoTM
361 Agar, BD) supplemented with ampicillin (100 µg/ml). To construct the deletion mutants, we
362 utilized the SAT1 flipper tool⁵². Specifically, the upstream and downstream regions of the genes
363 of interest were amplified from the genomic DNA of *C. auris* strain B8441 with primers listed in
364 Table S1, and cloned into pSFS2 in a homodirectional way so that they flanked the
365 nourseothricin resistance marker (SAT1) and the *FLP* recombinase gene. To generate the
366 B9J08_001458 deletion cassette, the upstream homologous region was cloned into the
367 Xhol/KpnI-HF (NEB) digested pSFS2 plasmid using NEBuilder HiFi (NEB) as per manufacturer

368 instructions. The resulting constructs were isolated from the transformants, digested with SacI-HF and NotI-HF and the downstream region was cloned into the digested plasmid. To generate
369 the B9J08_004112 deletion cassette, the upstream homologous region was cloned into the
370 Apal/KpnI-HF (NEB) digested pSFS2 plasmid. Resulting constructs were isolated from the
371 transformants, digested with SacII and NotI-HF and the downstream region was cloned into the
372 digested plasmid. All inserts of the plasmids were verified by sequencing (Mix2Seq, Eurofins
373 genomics). To produce a linear deletion cassette, each plasmid was digested with KpnI-HF and
374 SacII for the B9J08_004112 deletion cassette and with StuI and Scal for the B9J08_001458
375 deletion cassette. Primers used to verify correct insertion of the upstream and downstream
376 regions are listed in Table S1.
377

379 *Strain construction.* For strain construction, *C. auris* cells were prepared as described by Carolus
380 *et al.*⁵³. For electroporation, 40 µl of competent cells was mixed with the transformation mixture
381 and transferred to 2 mm electroporation cuvettes (Pulsestar, Westburg). The transformation
382 mixtures comprised 3 µl of 4 µM Alt-R™ S.p. Cas9 Nuclease V3, 3.6 µl of duplexed gene-specific
383 Alt-R® CRISPR-Cas9 crRNA (IDT) with Alt-R® CRISPR-Cas9 tracrRNA (IDT) and 500 ng of the
384 linearized constructed pSFS2 variant for each gene as donor DNA. A single pulse was given at
385 1.8 kV, 200 W, 25 mF, and the transformation mixture was immediately transferred to 2 ml YPD
386 in test tubes and incubated for 4 h at 37°C at 150 rpm. Cells were collected by centrifugation for
387 5 min at 5000 g, resuspended in 100 µl YPD and plated on YPD agar containing 200 µg/ml of
388 nourseothricin (Jena Bioscience). The sequences of the crRNA are listed in Table S1. Correct
389 transformants were screened by colony PCRs, using the Taq DNA Polymerase (NEB) and
390 primers that bind in the deletion cassette and outside of the homologous regions upstream and
391 downstream (Table S1). Null mutants of B9J08_001458 (*SCF1*) and B9J08_004112 (*ALS5*)
392 were generated in triplicate (3 independent transformants; $\Delta 1$ - $\Delta 3$) in both wild-type backgrounds
393 (AR0387 and AR0382) and evaluated for biofilm formation but only one representative mutant
394 was randomly selected for subsequent analysis (Fig. S2).
395

396 **Evaluation of potential complementary roles for the *Scf1* and *Als5* adhesins in surface
397 adhesion and biofilm formation.** To determine the impact of gene deletions on adherence and
398 biofilm formation and whether there are adherence complementary roles for the *Scf1* and *Als5*
399 adhesins, mutant strains were compared to the wild-type strain individually and in combination
400 in biofilm assays based on assessment of metabolic activity. Biofilms were grown by seeding
401 200 µl of 1×10^6 cells/ml cell suspensions of each strain in flat-bottom 96-well polystyrene
402 microtiter plates; for combination biofilms, mixed solutions of 100 µl of 1×10^6 cells/ml cell
403 suspensions of each mutant were used. Following incubation at 37°C for 24 h, wells were
404 washed with PBS and biofilms evaluated using the MTS metabolic assay (Promega) as per
405 manufacturer recommendation. Color intensity was measured at 490nm using a Cell Imaging
406 Multi-Mode Reader (Cytation 5, Biotek). Assays were performed on 3 separate occasions, each
407 using 4 technical replicates.
408

409 **Evaluation of potential complementary roles for the *Scf1* and *Als5* adhesins in cell-cell
410 adherence and coaggregation.** The contribution of adhesins to cell-cell interaction and
411 coaggregation was comparatively assessed based on formation of cell aggregates. For
412 coaggregation assays, cell suspensions of wild-type strain and mutant strains were suspended
413 in PBS to final density of 5×10^8 cells/ml in 5 ml plastic tubes, and suspensions vigorously

414 vortexed for 1 min. To evaluate adherence complementation of adhesins, suspensions of both
415 mutants at 2.5×10^8 cells/ml were equally mixed and vortexed. Tubes were placed upright at RT
416 and cell aggregation was monitored and imaged. Additionally, sedimentation rate of formed cell
417 aggregates was also measured based on drop in absorbance readings of cell suspensions. For
418 these experiments, aliquots from cell suspensions were measured at 600nm every 10 min for
419 up to 2 h in a BioTek 800 TS absorbance reader. Sedimentation rate was calculated as the
420 percent reduction in absorbance at each timepoint compared to the initial reading.
421

422 **Confocal laser scanning microscopy (CLSM) and scanning electron microscopy (SEM)**
423 **analysis of biofilms of wild-type and the $\Delta scf1$ and $\Delta als5$ mutants grown individually and**
424 **in combination.** For CLSM, biofilms of wild-type and mutant strains individually and in
425 combination were grown on glass coverslip-bottom dishes (MatTek Co., Ashland, MA) for 24 h; biofilms
426 were rinsed in PBS then stained with a concanavalin-A conjugated to Alexa 647 (Invitrogen) (50 μ g/ml) for 45 min at 37°C. Biofilms were visualized using an inverted confocal
427 laser scanning microscope (T2i, Nikon) and images analyzed using Imaris 9.3 Arena software
428 and ImageJ. For SEM, biofilms were grown on coverslips for 24 h at 37°C then fixed in 2%
429 paraformaldehyde-2.5% glutaraldehyde, post-fixed with 1% osmium tetroxide, serially
430 dehydrated in ethyl alcohol (30-100%) and critical-point dried. Samples were carbon-coated and
431 observed with Quanta 200 SEM (FEI Co.) and images processed using Adobe Photoshop
432 software.
433

434
435 ***In vivo* evaluation of AR0382 and AR0387 wild-type strains and $\Delta scf1$ mutant in a mouse**
436 **subcutaneous catheter model.** Based on observed *in vitro* biofilm deficiency of the $\Delta scf1$
437 mutant, its ability to form biofilm on catheters *in vivo* was evaluated in the subcutaneous catheter
438 model. The adherence of $\Delta scf1$ was compared to both the aggregative (AR0382) and non-
439 aggregative (AR0387) wild-type strains. For these experiments, catheter fragments inoculated
440 with the strains *in vitro* were implanted in animals as described above. Biofilms were allowed to
441 form within catheters for 72 h then animals were euthanized and catheters harvested. To
442 visualize the biofilms formed within the catheter lumen, catheters from each group were cut
443 longitudinally to expose the lumen, fixed and processed for SEM analysis as described above.
444 Catheters from 6 mice were analyzed and representative images presented.
445

446 **Comparative evaluation of cell-cell adhesion forces between cells of *C. auris* strains**
447 **using single-cell force spectroscopy (SCFS).** SCFS was employed to measure single cell-
448 cell adhesion forces among cells of wild-type and the two mutants⁵⁴⁻⁵⁶. For these studies, a single
449 live cell was attached to a polydopamine-coated tipless AFM cantilever and approached toward
450 another single cell, previously immobilized on a dish. The retraction and approach movement of
451 the cell probe was monitored and force-distance curves recorded, allowing quantification of the
452 forces driving intercellular adhesion. Triangular tipless cantilevers (NP O10, Bruker) were
453 immersed for 1 h in Tris-buffered saline solution (50 mM Tris, 150 mM NaCl, pH 8.5) containing
454 4 mg/ml of dopamine hydrochloride, rinsed with Tris-buffered saline solution and mounted on
455 the AFM setup for cell probe preparation. Calibration of the probe was performed prior to the
456 AFM experiment and its nominal spring constant determined by the thermal noise method. *C.
457 auris* cells were grown overnight in liquid YPD at 37°C, 150 rpm, harvested by centrifugation,
458 washed three times in 1X PBS and finally diluted 1000-fold. Cell suspensions were allowed to
459 adhere to polystyrene dishes for 20 min and dishes washed three times then filled with 2 ml of

460 1X PBS before being transferred to the AFM setup. SCFS measurements were performed at RT
461 in 1xPBS, using a Nanowizard 4 AFM (JPK Instrument, Berlin, Germany). The cell probe was
462 prepared by bringing the polydopamine-coated cantilever into contact with an isolated cell and,
463 once the probe was retracted, its attachment to the cantilever was confirmed using an inverted
464 optical microscope. The cell probe was then positioned over an immobilized cell and force maps
465 of 16x16 pixels were recorded on top of it, using a contact force setpoint of 250 pN, a constant
466 approach and retraction speeds of 1 μ m/s and an additional pause at contact of 1 s. Adhesion
467 forces were extracted from force-distance retraction curves by considering the rupture event for
468 which the adhesion force was maximal, for every curve.

469
470 **Data analysis.** Statistical analysis of biofilm growth was performed using R statistical
471 programming software. Statistical analysis of SCFS data was performed with Origin software
472 (OriginPro 2021). To compare differences among strains in *in vitro* biofilm forming capabilities
473 and cell-cell adhesion force and frequency, a one-way ANOVA with Tukey's post host test was
474 used. *P* values less than 0.05 were considered significant. Two-sample t-tests were used to
475 compare absorbance values, adhesion force and adhesion frequency between AR0382 and
476 AR0387 strains. Ggplot2 and ggpubr packages were used to construct models for figure
477 construction.

478
479 **DATA AVAILABILITY.** Upon acceptance and prior to publication, all of the raw sequencing
480 reads from this study will be available at the NCBI Sequence Read Archive (SRA). All strains
481 generated in this study will be made available upon request from authors.

482
483 **ACKNOWLEDGEMENTS.** The work in this publication was supported by the National Institute
484 of Allergy and Infectious Diseases of the NIH under award number R01AI130170 (NIAID) to
485 M.A.J-R, and NIH grant U19 AI110820 to V.M.B. This work was also supported by the University
486 of Maryland Baltimore, Institute for Clinical & Translational Research (ICTR), the Fund for
487 Scientific Research, Flanders, research community on biofilms (FWO #W000921N), and the
488 Belgian National Fund for Scientific Research (FNRS). We would like to thank Miles Delmar and
489 the UMB Electron Microscopy Core for SEM imaging.

490
491
492 **Author Contributions.**
493
494 M.A.J-R. and P.V.D. conceived and designed this research, M.A.J-R., V.M.B. and P.V.D.
495 provided funding; T.W.W., D.M-J., D.S., H.C., C.M., A.A. and T.O.P. performed experiments;
496 M.A.J-R., T.W.W., D.S., T.O.P., V.M.B., P.V.D., D.M-J. and Y.F.D. analyzed data; M.A.J-R.,
497 T.W.W., D.S., T.O.P., H.C. and V.M.B. wrote the paper; M.A.J-R. oversaw the entire study.

498
499 All authors read and approved the manuscript

500
501
502
503
504
505 **REFERENCES**

506

507 1. Vila, T., Sultan, A.S., Montelongo-Jauregui, D. & Jabra-Rizk, M.A. *Candida auris*: A
508 fungus with identity crisis *Pathog Dis* **78**, ftaa034 (2020).

509 2. Lockhart, S.R. *et al.* Simultaneous emergence of multidrug-resistant *Candida auris* on 3
510 continents confirmed by whole-genome sequencing and epidemiological analyses. *Clin
511 Infect Dis* **64**, 134–140 (2017).

512 3. Cortegiani, A., Misseri, G., Giarratano, A., Bassetti, M. & Eyre, D. The global challenge
513 of *Candida auris* in the intensive care unit. *Crit Care Med.* **23**, 150 (2019).

514 4. Lyman, M. *et al.* Worsening Spread of *Candida auris* in the United States, 2019 to 2021.
515 *Ann Intern Med* **176**, 489-495 (2023).

516 5. de Jong, A.W. & Hagen, F. Attack, defend and persist: How the fungal pathogen *Candida
517 auris* was able to emerge globally in healthcare environments. *Mycopathologia*. **148**, 353-
518 365. (2019).

519 6. Wickes, B.L. Analysis of a *Candida auris* outbreak provides new insights into an emerging
520 pathogen. *J Clin Microbiol* doi: [10.1128/JCM.02083-19](https://doi.org/10.1128/JCM.02083-19), pii: JCM.02083-02081 (2020).

521 7. Lockhart, S.R. *Candida auris* and multidrug resistance: Defining the new normal. *Fungal
522 Genet Biol.* **131**, doi: [10.1016/j.fgb.2019.103243](https://doi.org/10.1016/j.fgb.2019.103243) (2019).

523 8. Chaabane, F., Graf, A., Jequier, L. & Coste, A.T. Review on antifungal resistance
524 mechanisms in the emerging pathogen *Candida auris*. *Front Microbiol* **10**, 2788 (2019).

525 9. Carolus, H. *et al.* Genome wide analysis of experimentally evolved *Candida auris* reveals
526 multiple novel mechanisms of multidrug resistance. *mBio* **12**, e03333-03320 (2021).

527 10. Horton, M.V., Holt, A.M. & Nett, J.E. Mechanisms of pathogenicity for the emerging
528 fungus *Candida auris*. *PLoS Pathog* **19**, e1011843 (2023).

529 11. Fisher, M.C. *et al.* Tackling the emerging threat of antifungal resistance to human health.
530 *Nat Rev Microbiol* **20**, 557-571 (2022).

531 12. Harris, E. *Candida auris* fungal infections and drug resistance on the rise. *JAMA* **329**,
532 1248 (2023).

533 13. Fisher, M.C. & Denning, D.W. The WHO fungal priority pathogens list as a game-changer.
534 *Nat Rev Microbiol* **21**, 211-212 (2023).

535 14. Larkin, E. *et al.* The emerging pathogen *Candida auris*: Growth phenotype, virulence
536 factors, activity of antifungals, and effect of SCY-078 on growth morphology and biofilm
537 formation., a novel glucan synthesis inhibitor *Antimicrob Agents Chemother.* **61**, pii:
538 e02396-02316. (2017).

539 15. Sherry, L. *et al.* Biofilm-forming capability of highly virulent, multidrug-resistant *Candida
540 auris*. *Emerg Infect Dis.* **23**, 328-331 (2017).

541 16. Vila, T. *et al.* Comparative evaluations of the pathogenesis of *Candida auris* phenotypes
542 and *Candida albicans* using clinically relevant murine models of infections. *mSphere* **5**
543 (2020).

544 17. Kean, R. *et al.* Transcriptome asembly and profiling of *Candida auris* reveals novel
545 insights into biofilm-mediated resistance. *mSphere* **3**, e00334-00318 (2018).

546 18. Willaert, R.G., Kayacan, Y. & Devreese, B. The Flo adhesin family. *Pathogens* **10**, 1397
547 (2021).

548 19. Dominguez, E.G. *et al.* Conserved role for biofilm matrix polysaccharides in *Candida auris*
549 drug resistance. *mSphere* **4**, pii: e00680-00618. (2019).

550 20. Brown, J.L. *et al.* *Candida auris* phenotypic heterogeneity determines pathogenicity in
551 vitro *mSphere* **5**, e00371-00320 (2020).

552 21. Short, B. *et al.* *Candida auris* exhibits resilient biofilm characteristics *in vitro*: Implications
553 for environmental persistence. *J Hosp Infect* **103**, 92-96 (2019).

554 22. Szekely, A., Borman, A.M. & Johnsona, E.M. *Candida auris* isolates of the southern asian
555 and south african lineages exhibit different phenotypic and antifungal susceptibility
556 profiles in vitro. *J Clin Microbiol* **57**, 1-12 (2019).

557 23. de Groot, P.W., Bader, O., de Boer, A.D., Weig, M. & Chauhan, N. Adhesins in human
558 fungal pathogens: glue with plenty of stick. *Eukaryot Cell* **12**, 470-481 (2013).

559 24. Sundstrom, P. Adhesion in *Candida* spp. *Cell Microbiology* **4**, 461-469 (2002).

560 25. Dehullu, J. *et al.* Fluidic force microscopy demonstrates that homophilic adhesion by
561 *Candida albicans* Als proteins is mediated by amyloid bonds between cells. *Nano Lett*
562 **19**, 3846-3853 (2019).

563 26. Malavia-Jones, D. *et al.* Strain and temperature dependent aggregation of *Candida auris*
564 is attenuated by inhibition of surface amyloid proteins. *Cell Surf* **10** (2023).

565 27. Bing , J. *et al.* Clinical isolates of *Candida auris* with enhanced adherence and biofilm
566 formation due to genomic amplification of *ALS4*. *PLoS Pathog* **19**, e1011239 (2023).

567 28. Santana, D.J. *et al.* A *Candida auris*-specific adhesin, *Scf1*, governs surface association,
568 colonization, and virulence. *Science* **381**, 1461-1467 (2023).

569 29. Nobile, C.J. *et al.* Complementary adhesin function in *C. albicans* biofilm formation. *Curr*
570 *Biol* **18**, 1017-1024 (2008).

571 30. Soll, D.R. The role of phenotypic switching in the basic biology and pathogenesis of
572 *Candida albicans*. *J Oral Microbiol* **6** (2014).

573 31. Kim, S.H. *et al.* Genetic analysis of *Candida auris* implicates Hsp90 in morphogenesis
574 and azole tolerance and Cdr1 in azole resistance. *mBio*. **10**, pii: e02529-02518 (2019).

575 32. Viljoen, A. *et al.* Force spectroscopy of single cells using atomic force microscopy. *Nat*
576 *Rev Methods Primers* **1** (2021).

577 33. Alsteens, D., Garcia, M.C., Lipke, P.N. & Dufrêne, Y.F. Force-induced formation and
578 propagation of adhesion nanodomains in living fungal cells. *Proc Natl Acad Sci U S A*
579 **107**, 20744-20749 (2010).

580 34. Skrzypek, M.S. *et al.* The Candida Genome Database (CGD): Incorporation of Assembly
581 22, systematic identifiers and visualization of high throughput sequencing data. *Nucleic*
582 *Acids Res* **45**, D592-D596 (2017).

583 35. Muñoz, J.F. *et al.* Clade-specific chromosomal rearrangements and loss of subtelomeric
584 adhesins in *Candida auris*. *Genetics*. **218**, iyab029 (2021).

585 36. Balakumar, A., Bernstein, D. & Thangamani, S. The adhesin *SCF1* mediates *Candida*
586 *auris* colonization. *Trends Microbiol* **32**, 4-5 (2024).

587 37. Monniot, C. *et al.* Rbt1 protein domains analysis in *Candida albicans* brings insights into
588 hyphal surface modifications and Rbt1 potential role during adhesion and biofilm
589 formation. *PLoS One* **8**, e82395 (2013).

590 38. Ene, I.V. & Bennett, R.J. Hwp1 and related adhesins contribute to both mating and biofilm
591 formation in *Candida albicans*. *Eukaryot Cell* **8**, 1909-1913 (2009).

592 39. Nobile, C.J., Nett, J.E., Andes, D.R. & Mitchell, A.P. Function of *Candida albicans* adhesin
593 Hwp1 in biofilm formation. *Eukaryot Cell* **5**, 1604-1610 (2006).

594 40. Rauceo, J.M. *et al.* Global cell surface conformational shift mediated by a *Candida*
595 *albicans* adhesin. *Infect Immun* **72**, 4948-4955 (2004).

596 41. Hoyer, L.L., Green, C.B., Oh, S.H. & Zhao, X. Discovering the secrets of the *Candida*
597 *albicans* agglutinin-like sequence (ALS) gene family-a sticky pursuit. *Med Mycol* **46**, 1-15
598 (2008).

599 42. Gaur, N.K., Klotz, S.A. & Henderson, R.L. Overexpression of the *Candida albicans* ALA1
600 gene in *Saccharomyces cerevisiae* results in aggregation following attachment of yeast
601 cells to extracellular matrix proteins, adherence properties similar to those of *Candida*
602 *albicans*. *Infect Immun* **67**, 6040-6047 (1999).

603 43. Gaur, N.K., Smith, R.L. & Klotz, S.A. *Candida albicans* and *Saccharomyces cerevisiae*
604 expressing ALA1/ALS5 adhere to accessible threonine, serine, or alanine patches. *Cell*
605 *Commun Adhes* **9**, 45-57 (2002).

606 44. Klotz, S.A. *et al.* Degenerate peptide recognition by *Candida albicans* adhesins Als5p and
607 Als1p. *Infect Immun* **72**, 2029-2034 (2004).

608 45. Dehullu, J., Vorholt, J.A., Lipke, P.N. & Dufrêne, Y.F. Fluidic force microscopy captures
609 amyloid bonds between microbial cells. *Trends Microbiol* **27**, 728-730 (2019).

610 46. Lipke, P.N., Klotz, S.A., Dufrene, Y.F., Jackson, D.N. & Garcia-Sherman, M.C. Amyloid-
611 like β -aggregates as force-sensitive switches in fungal biofilms and infections. *Microbiol*
612 *Mol Biol Rev* **82**, e00035 (2017).

613 47. Mourer, T., El Ghalid, M., d'Enfert, C. & Bachellier-Bassi, S. Involvement of amyloid
614 proteins in the formation of biofilms in the pathogenic yeast *Candida albicans*. *Res*
615 *Microbiol* **172**, 103813 (2021).

616 48. Carolus, H. *et al.* Diagnostic Allele-Specific PCR for the Identification of *Candida auris*
617 Clades. *J Fungi (Basel)* **7**, 754 (2021).

618 49. Kim, D., Paggi, J.M., Park, C., Bennett, C. & Salzberg, S.L. Graph-based genome
619 alignment and genotyping with HISAT2 and HISAT-genotype. *Nat Biotechnol* **37**, 907-
620 915 (2019).

621 50. Anders, S. & Huber, W. Differential expression analysis for sequence count data.
622 *Genome Biol* **11** (2010).

623 51. Kucharíková, S., Tournu, H., Holtappels, M., Van Dijck, P., Lagrou, K. *In vivo* efficacy of
624 anidulafungin against mature *Candida albicans* biofilms in a novel rat model of catheter-
625 associated candidiasis. *Antimicrob. Agents Chemother.* **54** 4474-4475 (2010).

626 52. Reuss, O., Vik, A., Kolter, R. & Morschhäuser, J. The SAT1 flipper, an optimized tool for
627 gene disruption in *Candida albicans*. *Gene* **119-27** (2004).

628 53. Carolus, H., Sofras, D., Boccarella, G. & Sephton-Clark, P. Acquired amphotericin B
629 resistance and fitness trade-off compensation in *Candida auris*. *preprint*
630 <https://doi.org/10.21203/rs.3.rs-3621420/v1> (2024).

631 54. Viljoen, A., Mathelié-Guinlet, M. & Ray, A. Force spectroscopy of single cells using atomic
632 force microscopy. *Nat Rev Methods Primers* **1** (2021).

633 55. Alsteens, D., Van Dijck, P., Lipke, P.N. & Dufrêne, Y.F. Quantifying the forces driving
634 cell-cell adhesion in a fungal pathogen *Langmuir* **29**, 13473-13480 (2013).

635 56. Alsteens, D. *et al.* Single-cell force spectroscopy of Als-mediated fungal adhesion *Anal*
636 *Methods* **3**, 3657-3662 (2013).

637
638
639
640 **FIGURE LEGEND**
641

642 **Fig. 1. RNA-seq analysis of *in vitro* and *in vivo* grown biofilms depicting genes**
643 **differentially regulated in the aggregative *C. auris* strain AR0382 compared to the non-**
644 **aggregative strain AR0387.** Volcano plots of comparative differential gene expressions during
645 **(A) *in vitro* and (B) *in vivo* biofilm growth. LFC, log (base 2) fold change. FDR, false-discovery**
646 **rate. Black: not statistically significant (FDR > 0.01); Red: Statistically significant (FDR < 0.01);**
647 **Purple: Statistically significant and an adhesin. (C) Venn diagrams representing the overlap in**
648 **the numbers of genes that are more highly expressed in strain AR0382 *in vitro* and *in vivo*.**

649
650 **Figure 2. Scf1 adhesin domain organization.** Diagram comparing the *C. auris* Scf1 domain
651 structure to that of the *C. albicans* Rbt1 adhesin and the *Saccharomyces cerevisiae* Flo11
652 depicting a common Flo11 domain and a serine-threonine rich region (>50%) recognized by
653 Als5. Pfam database code is in parentheses; signal peptides and GPI-anchors were predicted
654 using the prediction softwares SignalP 6.0 and NetGPI-1.1, respectively. Functional domains of
655 adhesin proteins were identified via InterProtScan
656 (<https://www.ebi.ac.uk/interpro/search/sequence/>) (accessed February 12, 2024). Uniprot
657 entries: A0A2H1A319 (Scf1); A0A8H6F4R1 (Rbt1); P08640 (Flo11); A0A2H0ZH9 (Als5).

658
659 **Figure 3. Comparative evaluation of biofilm formation, aggregation and sedimentation**
660 **rate of Δ scf1 and Δ als5 mutants individually and in combination compared to the wild-**
661 **type (AR0382). (A)** Measurement of the metabolic activity of 24 h biofilms based on values of
662 OD₄₉₀ comparing wild-type AR0382 to Δ scf1 and Δ als5 mutants and Δ scf1+ Δ als5 combination.
663 Statistical analysis was performed by one-way ANOVA and post-hoc Tukey test with *p*-values
664 representing significant differences. Bar-plots show mean and SEM of *n* = 3 biological replicates,
665 each as an average of 4 technical replicates. *P* = 2.61 \times 10⁻³, 1.75 \times 10⁻³. **(B)** Cell aggregation 2
666 min after vigorous vortexing and **(C)** 10 min post-vortexing. **(D)** Measurement of rate of cell
667 sedimentation over 2 hr. Values represented are mean OD plus SEM of three technical
668 replicates. **0.001 < *P* \leq 0.01.

669
670 **Figure. 4. Representative images from confocal laser scanning microscopy analysis of**
671 **biofilms formed by the *C. auris* AR0382 wild-type (WT) strain and the Δ scf1 and Δ als5**
672 **mutants grown individually and in combination (Δ scf1+ Δ als5).** Z-stack reconstructions of
673 biofilms stained with polysaccharide stain concanavalin A (fuchsia).

674
675 **Figure. 5. Representative images from scanning electron microscopy analysis.** 24 h
676 biofilms formed by the *C. auris* AR0382 wild-type (WT) strain and the Δ scf1 and Δ als5 mutants
677 grown individually and in combination (Δ scf1+ Δ als5).

678
679 **Figure 6. Single-cell force spectroscopy of *C. auris* cell-cell adhesion.** **(A)** Adhesion force
680 histograms with representative retraction profiles (inset) obtained for the interaction between
681 AR0382 wild-type cells, cells of Δ als5, cells of Δ scf1 and between cells of Δ als5 and Δ scf1
682 (Δ als5+ Δ scf1); 2 representative cell pairs are shown for each strain. **(B)** Adhesion force boxplots
683 show data on *n* = 6 pairs of AR0382 cells, Δ als5 cells, and Δ scf1 cells and *n* = 8 cell pairs
684 combining Δ als5 and Δ scf1. Statistical analysis was performed by one-way ANOVA and post-
685 hoc Tukey test with *p*-values representing significant differences. *P* = 1.42 \times 10⁻², 7.69 \times 10⁻³,
686 1.01 \times 10⁻². **(C)** As in **(B)**, adhesion frequency boxplots show data on *n* = 7 pairs of AR0382 cells,
687 *n* = 5 pairs of Δ als5 cells, *n* = 6 pairs of Δ scf1 cells and *n* = 8 pairs between Δ als5+ Δ scf1 cells.
688 *P*=1.71 \times 10⁻³, 3.77 \times 10⁻². Red stars represent the mean values, red lines are the medians, boxes

688 are the 25–75% quartiles and whiskers the standard deviation from mean. * $0.01 < P \leq 0.05$,
689 ** $0.001 < P \leq 0.01$.

690

691 **Figure. 7. Infection and biofilm formation in catheters implanted in mice. (A)** A small
692 incision is made in a shaved area in the dorsum of anesthetized mice and catheter fragments
693 (0.5 cm) are inserted within a formed subcutaneous tunnel. **(B)** Scanning electron microscopy
694 of explanted catheters. Representative low- and high-magnification SEM images demonstrating
695 mature biofilm formed within lumen of catheters infected with AR0382 wild-type strain consisting
696 of aggregates of yeast cells.

697

698 **Figure. 8. Hypothetical mechanistic model depicting complementary Scf1/Als5 binding.**
699 (left) Adherence between wild-type (WT) cells involving Scf1+Als5 complementary binding and
700 homophilic interactions between Als5+Als5 and Scf1+Scf1; (right) Complementary binding
701 between Scf1 and Als5 on the Δ als5 and Δ scf1 mutant cells, respectively. Domain designations
702 and colors are consistent with those in Fig. 2.

703

704 Supplemental Material

705

706 **Supplemental Figure S1. Probing *C. auris* cell-cell adhesion using single-cell force**
707 **spectroscopy.** AFM setup used for single-cell force spectroscopy experiments. A single live *C.*
708 *auris* cell was attached to a tipless AFM cantilever previously functionalized with polydopamine.
709 This cell probe was moved toward another single *C. auris* cell immobilized on a polystyrene dish
710 and force-distance curves were recorded, allowing quantification of the intercellular adhesion
711 forces.

712

713 **Supplemental Figure S2. Evaluation of biofilm formation by the 3 mutant strains**
714 **generated for the ALS5 and SCF1 genes (Δ1-Δ3).** A measurement of the metabolic activity of
715 24 h biofilms based on values of OD₄₉₀ comparing all generated mutant strains to the wild-type.
716 Boxplots show mean and SEM of $n = 3$ biological replicates, each as an average of 4 technical
717 replicates. Statistical analysis was performed by one-way ANOVA and post-hoc Tukey test with
718 p -values representing significant differences. $P=1.64\times10^{-3}$, 1.55×10^{-3} , 2.18×10^{-3} , 2.02×10^{-4} ,
719 3.70×10^{-4} , 3.50×10^{-4} , 4.83×10^{-4} , 5.17×10^{-5} , 3.35×10^{-4} , 3.17×10^{-4} , 4.37×10^{-4} , 4.71×10^{-5} ** $0.001 < P \leq 0.01$, *** $P < 0.001$.

721

722 **Supplemental Figure S3. Comparative evaluation of biofilm formation, aggregation and**
723 **cell-cell adhesion force by the wild-type AR0382 (aggregative) and AR0387 (non-**
724 **aggregative) phenotypes. (A)** Metabolic activity of 24 h biofilms based on measurements of
725 OD₄₉₀, optical density. Values are means plus standard errors of the means (error bars).
726 Statistical analysis was performed by an unpaired two-sided t-test. Bar-graphs shows mean and
727 SEM of $n = 3$ biological replicates, each as an average of 4 technical replicates. $P = 2.243\times10^{-5}$. **(B)**
728 Aggregation assays, following vigorous vortexing of cell suspensions comparing cell
729 aggregates of AR0382 and AR0387. Bright-field microscopy (lower panel) of aliquots of cell
730 suspensions demonstrating presence of aggregates of AR0382 cells compared to singly
731 suspended cells of AR0387. **(C)** Measurement of rate of cell sedimentation by absorbance
732 readings of OD₆₀₀ of wild-type strains AR0382 and AR0387 over 2 h following vigorous vortexing.
733 Values represent mean OD and SEM of three technical replicates. **(D)** Single-cell force

734 spectroscopy of *C. auris* cell-cell adhesion. Adhesion force histograms with representative
735 retraction profiles (inset) obtained for the interaction between AR0382 wild-type cells and the
736 interaction between AR0387 cells; 2 representative cell pairs are shown for each strain. **(E)**
737 Adhesion force boxplots depicting $n = 6$ and $n = 4$ cell pairs for AR0382 and AR0387
738 respectively. Statistical analysis was performed by an unpaired two-sided t-test. $P = 4.21 \times 10^{-2}$
739 **(F)** As in **(E)**, adhesion frequency boxplots show interactions between $n = 7$ cell pairs for both
740 strains. $P = 8.06 \times 10^{-6}$. Red stars represent the mean values, red lines are the medians, boxes
741 are the 25–75% quartiles and whiskers the standard deviation from mean. * $0.01 < P \leq 0.05$, *** P
742 < 0.001 .

743

744 **Table S1.** Primers used in this study

745

746 **Table S2.** Differentially expressed genes between AR0382/AR0387 during *in vitro* biofilm
747 growth (FDR <0.01 , LFC $\geq |1.0|$)

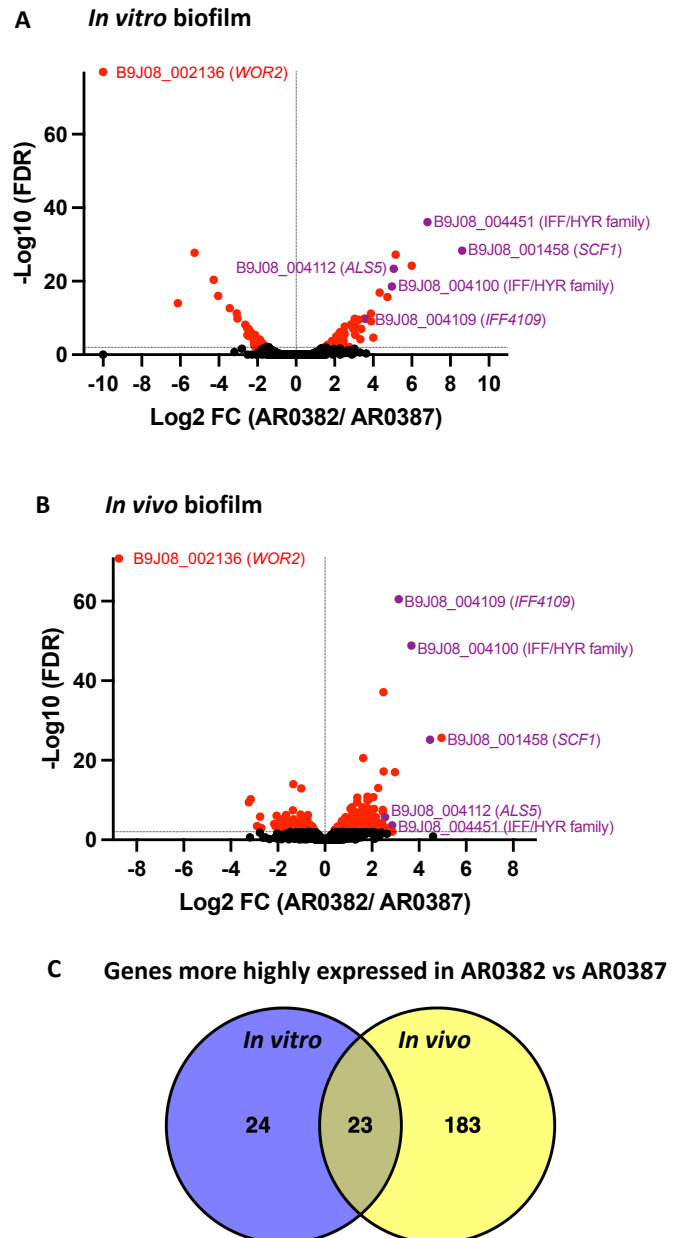
748

749 **Table S3.** Differentially expressed genes between AR0382/AR0387 during *in vivo* biofilm
750 growth (FDR <0.01 , LFC $\geq |1.0|$)

751

752 **Table S4.** List of genes that are more highly expressed in AR382 under both *in vitro* and *in*
753 *vivo* biofilm conditions (FDR <0.01 , LFC $\geq |1.0|$)

Figure. 1. RNA-seq analysis of *in vitro* and *in vivo* grown biofilms depicting genes differentially regulated in the aggregative *C. auris* strain AR0382 compared to the non-aggregative strain AR0387. Volcano plots of comparative differential gene expressions during (A) *in vitro* and (B) *in vivo* biofilm growth. LFC, log (base 2) fold change. FDR, false-discovery rate. *Black*: not statistically significant (FDR > 0.01); *Red*: Statistically significant (FDR < 0.01); *Purple*: Statistically significant and an adhesin. (C) Venn diagrams representing the overlap in the numbers of genes that are more highly expressed in strain AR0382 *in vitro* and *in vivo*.



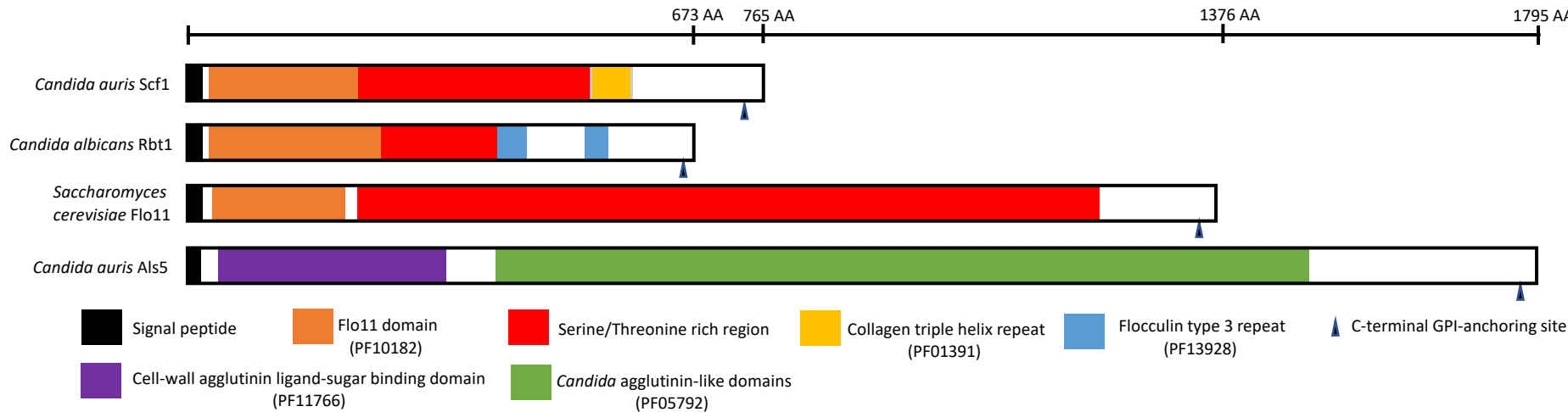


Figure. 2. Scf1 adhesin domain organization. Diagram comparing the *C. auris* Scf1 domain structure to that of the *C. albicans* Rbt1 adhesin and the *Saccharomyces cerevisiae* Flo11 depicting a common Flo11 domain and a serine-threonine rich region (>50%) recognized by Als5. Pfam database code is in parentheses; signal peptides and GPI-anchors were predicted using the prediction softwares SignalP 6.0 and NetGPI-1.1, respectively. Functional domains of adhesin proteins were identified via InterProtScan (<https://www.ebi.ac.uk/interpro/search/sequence/>) (accessed February 12, 2024). Uniprot entries: A0A2H1A319 (Scf1); A0A8H6F4R1 (Rbt1); P08640 (Flo11); A0A2H0ZH9 (Als5).

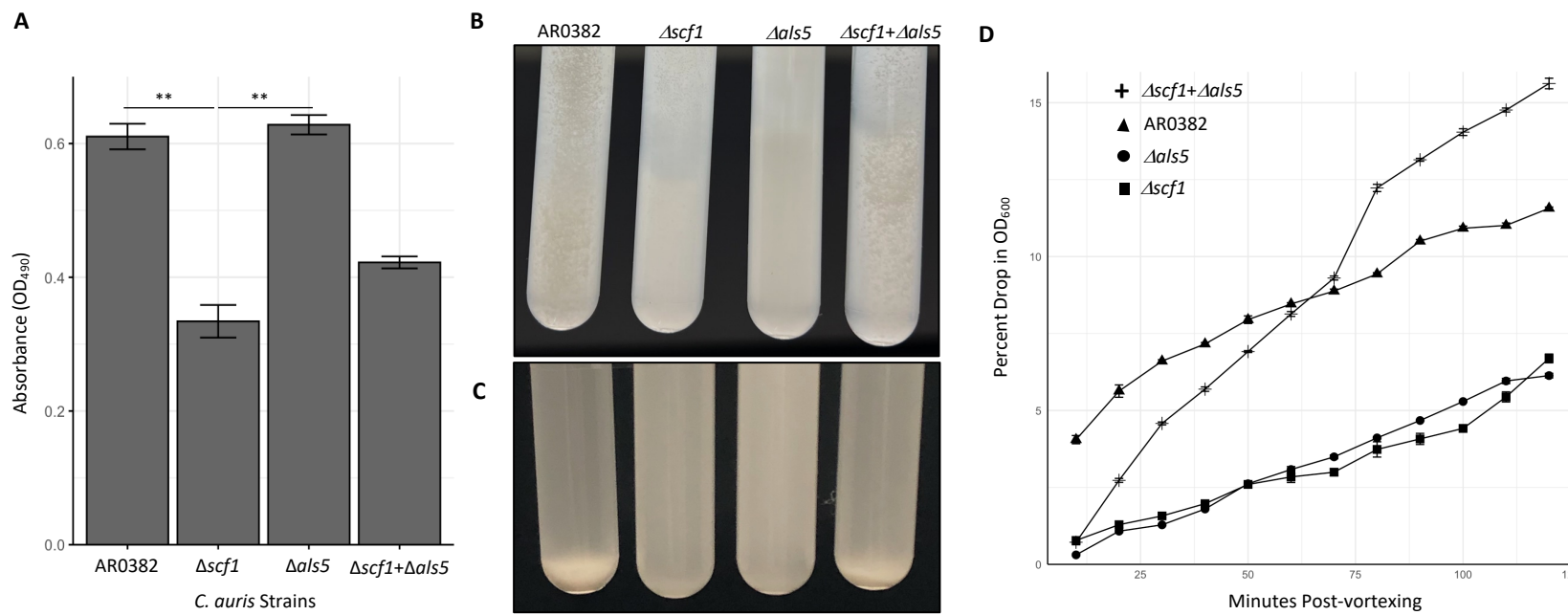


Figure 3. Comparative evaluation of biofilm formation, aggregation and sedimentation rate of $\Delta scf1$ and $\Delta als5$ mutants individually and in combination compared to the wild-type (AR0382). (A) Measurement of the metabolic activity of 24 h biofilms based on values of OD_{490} comparing wild-type AR0382 to $\Delta scf1$ and $\Delta als5$ mutants and $\Delta scf1+\Delta als5$ combination. Statistical analysis was performed by one-way ANOVA and post-hoc Tukey test with p -values representing significant differences. Bar-plots show mean and SEM of $n = 3$ biological replicates, each as an average of 4 technical replicates. $P = 2.61 \times 10^{-3}$, 1.75×10^{-3} . (B) Cell aggregation 2 min after vigorous vortexing and (C) 10 min post-vortexing. (D) Measurement of rate of cell sedimentation over 2 hr. Values represented are mean OD plus SEM of three technical replicates. ** $0.001 < P \leq 0.01$.

AR0382

$\Delta scf1$

$\Delta als5$

$\Delta scf1+\Delta als5$

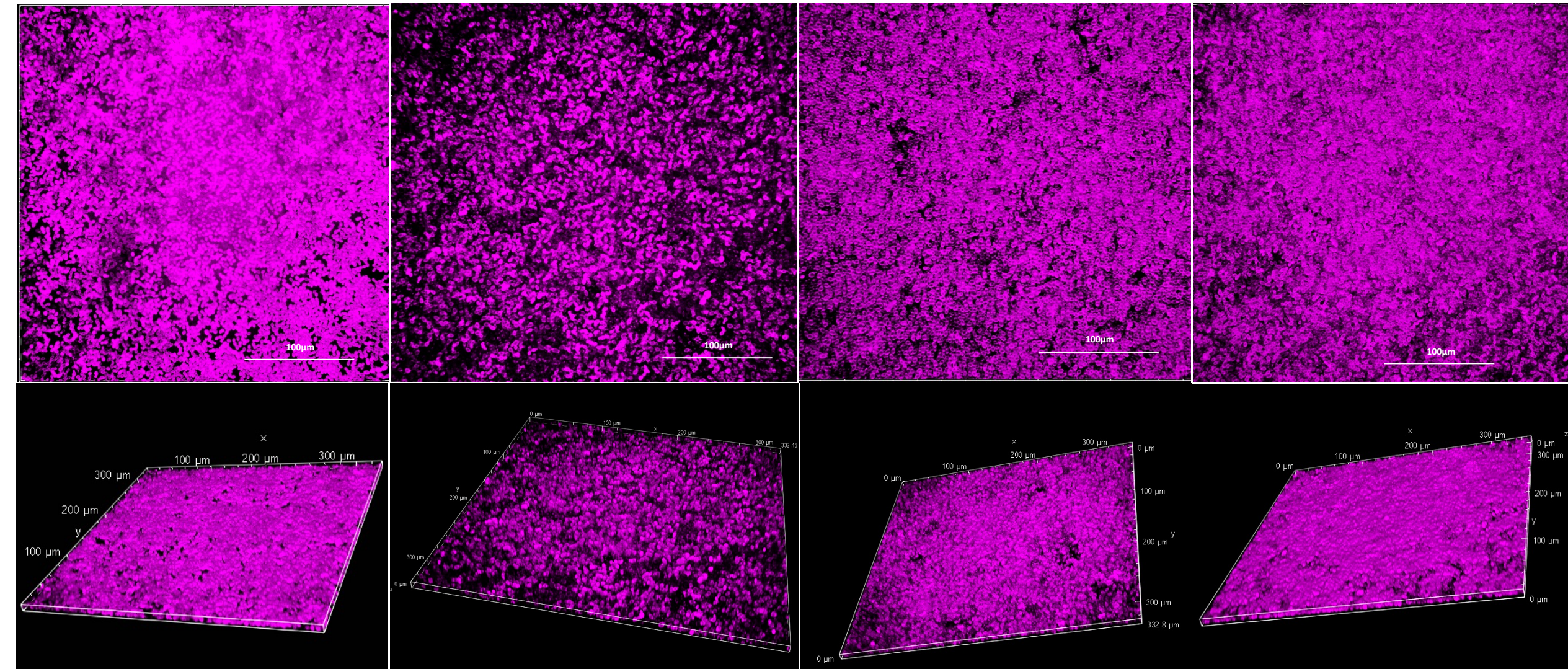


Figure 4. Representative images from confocal laser scanning microscopy analysis of biofilms formed by the *C. auris* AR0382 wild-type (WT) strain and the $\Delta scf1$ and $\Delta als5$ mutants grown individually and in combination ($\Delta scf1+\Delta als5$). Z-stack reconstructions of biofilms stained with polysaccharide stain concanavalin A (fuchsia).

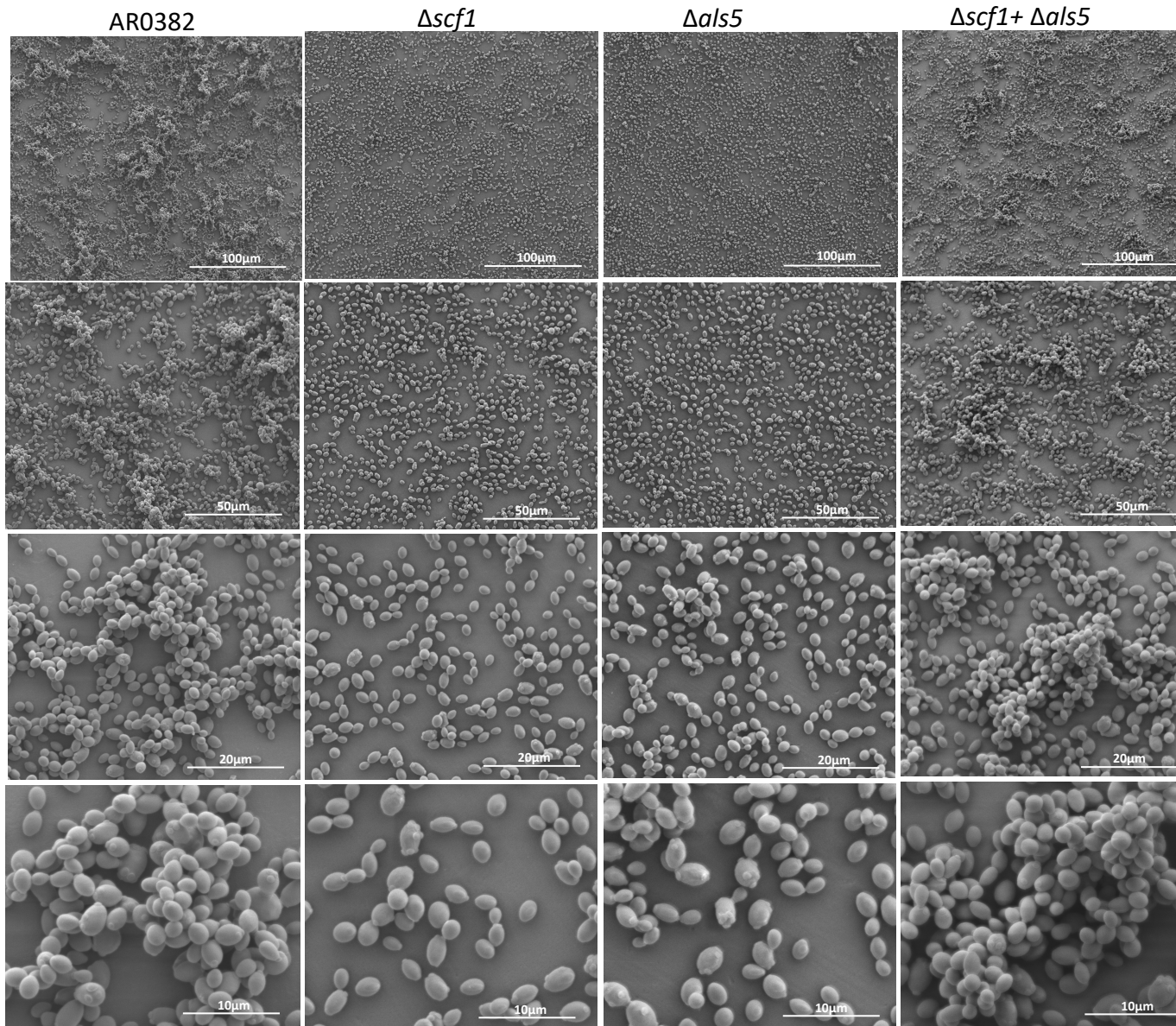


Figure 5. Representative images from scanning electron microscopy analysis. 24 h biofilms formed by the *C. auris* AR0382 wild-type (WT) strain and the $\Delta scf1$ and $\Delta als5$ mutants grown individually and in combination ($\Delta scf1 + \Delta als5$).

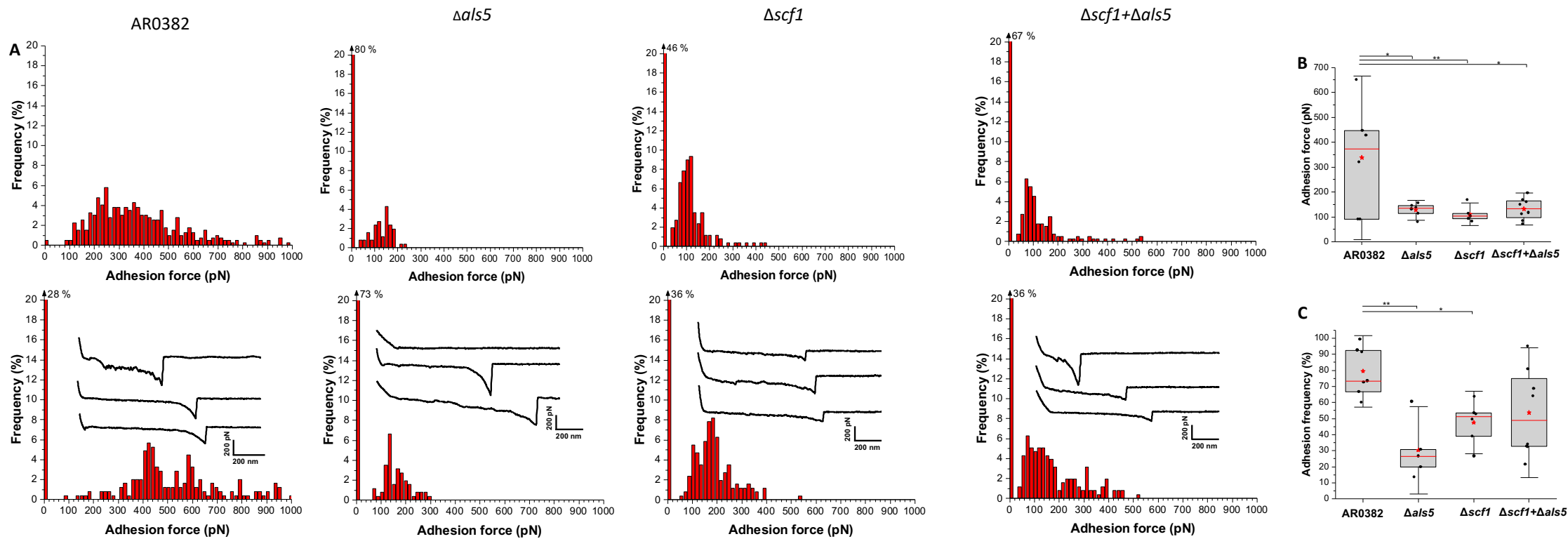


Figure 6. Single-cell force spectroscopy of *C. auris* cell-cell adhesion. (A) Adhesion force histograms with representative retraction profiles (inset) obtained for the interaction between AR0382 wild-type cells, cells of $\Delta als5$, cells of $\Delta scf1$ and between cells of $\Delta als5$ and $\Delta scf1$ ($\Delta als5+\Delta scf1$); 2 representative cell pairs are shown for each strain. (B) Adhesion force boxplots show data on $n = 6$ pairs of AR0382 cells, $\Delta als5$ cells, and $\Delta scf1$ cells and $n = 8$ cell pairs combining $\Delta als5$ and $\Delta scf1$. Statistical analysis was performed by one-way ANOVA and post-hoc Tukey test with p -values representing significant differences. $P = 1.42 \times 10^{-2}$, 7.69×10^{-3} , 1.01×10^{-2} . (C) As in (B), adhesion frequency boxplots show data on $n = 7$ pairs of AR0382 cells, $n = 5$ pairs of $\Delta als5$ cells, $n = 6$ pairs of $\Delta scf1$ cells and $n = 8$ pairs between $\Delta als5+\Delta scf1$ cells. $P=1.71 \times 10^{-3}$, 3.77×10^{-2} . Red stars represent the mean values, red lines are the medians, boxes are the 25–75% quartiles and whiskers the standard deviation from mean. * $0.01 < P \leq 0.05$, ** $0.001 < P \leq 0.01$.

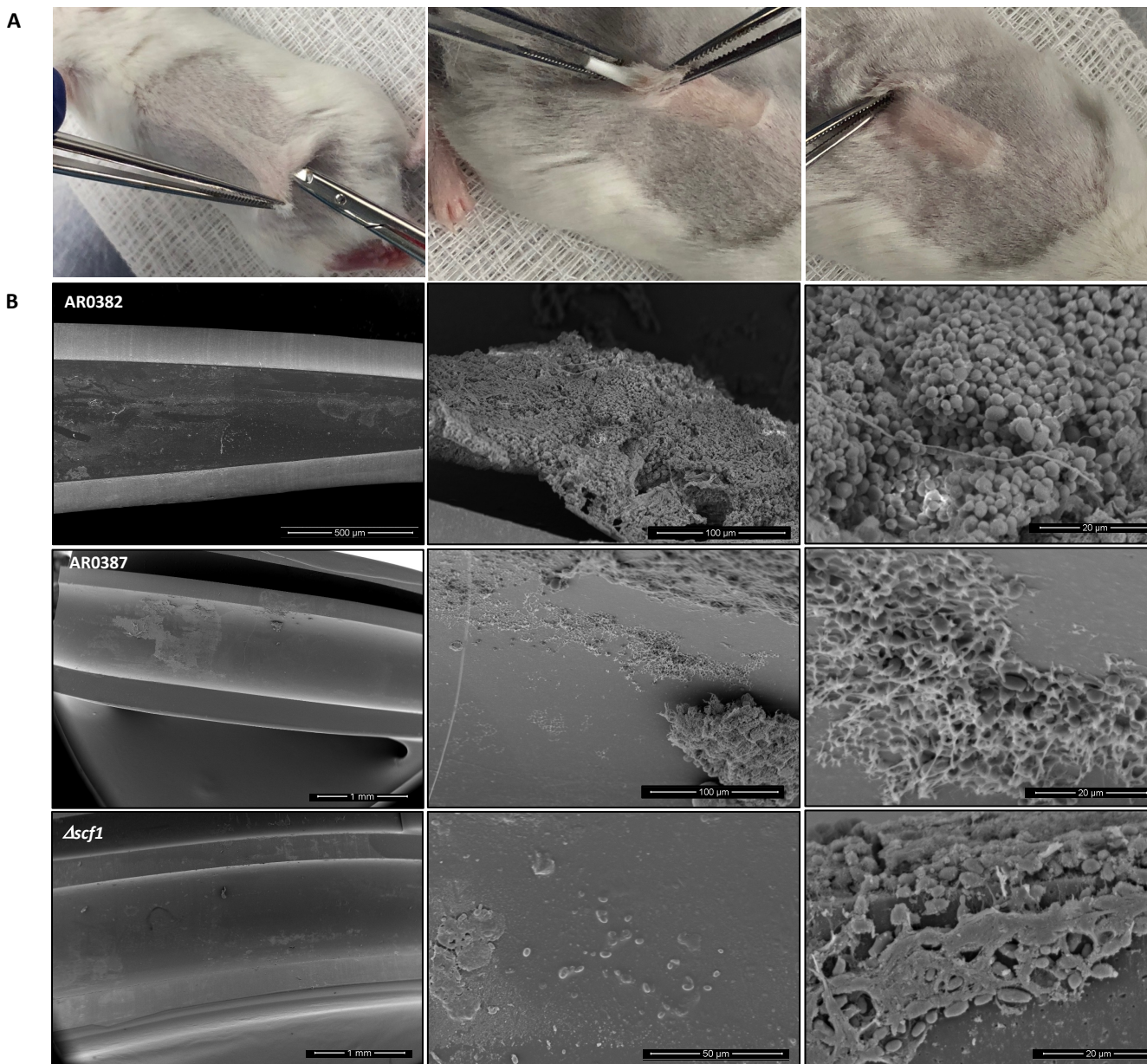


Figure. 7. Infection and biofilm formation in catheters implanted in mice. (A) A small incision is made in a shaved area in the dorsum of anesthetized mice and catheter fragments (0.5 cm) are inserted within a formed subcutaneous tunnel. **(B)** Scanning electron microscopy of explanted catheters. Representative low- and high-magnification SEM images demonstrating mature biofilm formed within lumen of catheters infected with AR0382 wild-type strain consisting of aggregates of yeast cells.

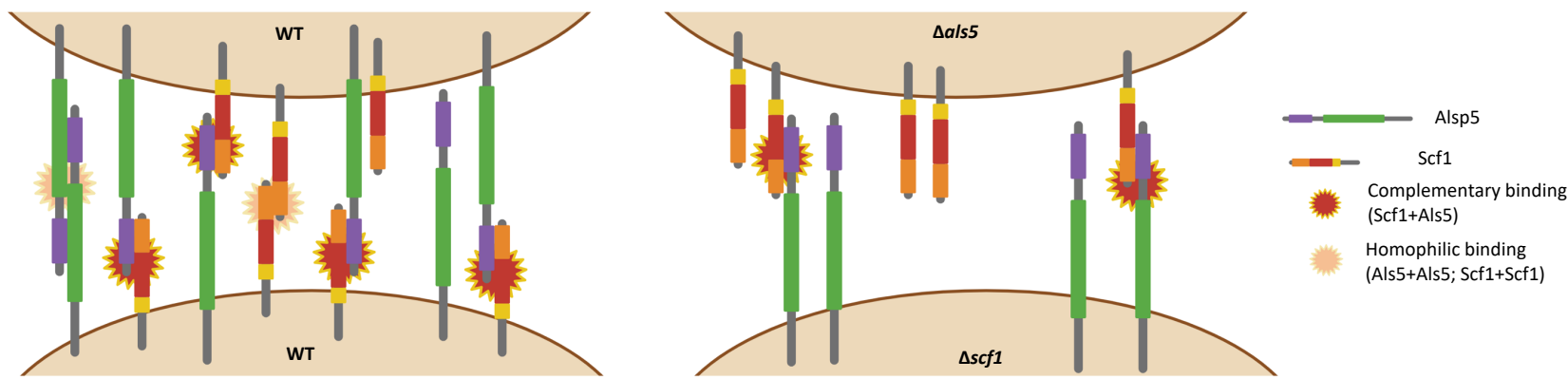


Figure. 8. Hypothetical mechanistic model depicting complementary Scf1/Als5 binding. (left) Adherence between wild-type (WT) cells involving Scf1+Als5 complementary binding and homophilic interactions between Als5+Als5 and Scf1+Scf1; **(right)** Complementary binding between Scf1 and Als5 on the $\Delta als5$ and $\Delta scf1$ mutant cells, respectively. Domain designations and colors are consistent with those in Fig. 2.